

A Local Hypersingular Boundary Integral Equation Method Using a Triangular Background Mesh

V. Vavourakis¹

Abstract: In this paper, a new meshless Local Hypersingular Boundary Integral Equation method is presented for the analysis of two-dimensional elastostatic problems. The elastic domain is discretized by placing arbitrarily nodes on its boundary and interior. Given this set of nodes, the corresponding map of background triangles is constructed through a common triangulation algorithm. The local domain of each node consists of the union of triangles that this point lies, thus, creating a polygonal line of its local boundary. The local boundary integral equations of both displacements and stresses of the conventional Boundary Elements Method are taken into account. The interpolation of the unknown fields is performed by taking each face of a triangle of the local domain of a source point as a one-dimensional line element. The essential boundary conditions can be directly implemented easily because the interpolation functions possess the Kronecker delta-function property. After constructing the final linear system of equations, the only unknowns are displacements and stresses of all nodal points. Thus, leading to a banded stiffness matrix as in the Finite Element Method. The effectiveness and efficiency of the proposed method is demonstrated with three elastostatic problems in two-dimensions. Excellent agreement between the numerical results and the exact solutions is found. The numerical examples also show that the accuracy of the proposed method is as good as that of the Boundary Elements Method.

Keyword: local hypersingular boundary integral equation, boundary elements, background triangles, meshless, elastostatics

1 Introduction

In the past two decades, mesh-free numerical methods for solving partial differential equations seem to attract more attention. The main reason why these methods attracted so much interest is that the task of meshing complex three-dimensional

¹ Institute of Applied and Computational Mathematics, Foundation for Research and Technology - Hellas, Heraklion Crete, Greece

geometries can be time-consuming, computationally cumbersome and expensive. The pioneering meshless methods are the Smooth Particle Hydrodynamic [Gingold and Moraghan (1977)], the Element-Free Galerkin (EFG) method [Belytschko, Lu, and Gu (1994)], the Reproducing Kernel Particle method [Liu, Jun, and Zhang (1995)], the Partition of Unity [Melenk and Babuška (1996)], the Meshless Local Petrov-Galerkin (MLPG) method [Atluri and Zhu (1998)], the Local Boundary Integral Equation (LBIE) method [Zhu, Zhang, and Atluri (1998)], the Natural Element Method (NEM) [Sukumar, Moran, and Belytschko (1998)], and the Point Interpolation Method [Wendland (1999)].

Some major advantages of the mesh-free methods are: (i) h-adaptivity is simpler to incorporate in these methods than in the Finite Element Method (FEM) [Duarte and Oden (1996)], (ii) moving discontinuities and phase transformations are treated with less effort, (iii) large-deformation analysis can be performed more efficiently [Chen, Pan, Wu, and Liu (1996)], (iv) higher-order continuous shape functions can be incorporated with the Moving Least Square (MLS) [Lancaster and Salkauskas (1981)] and Radial Basis Functions (RBF) [Wu (1995)], (v) non-local interpolation character and (vi) no mesh alignment sensitivity.

However like all other mesh-based numerical methods, meshless methods have their limitations. For instance, in the most widely used EFG and MLPG methods, the computational cost of evaluating the shape functions and their derivatives is much higher than that of the conventional FEM and Boundary Elements Method (BEM). The numerical evaluation of all boundary and volume integrals requires special care, due to the rational form of the shape functions and the complexity of the non-element interpolation. In addition, the essential boundary conditions cannot be enforced directly because the shape functions of MLS approximations do not possess the Kronecker delta-function property. Furthermore, the afore-mentioned meshless methods generate a sparse stiffness matrix and not a banded one as in FEM. In general, the time cost of meshless methods is higher than that of FEM and BEM.

The Local Boundary Integral Equation method has been implemented in various fields. The most representative works are found in potential problems [Zhu, Zhang, and Atluri (1998); Zhu (1999)], in two-dimensional linear elasticity [Atluri, Sladek, Sladek, and Zhu (2000); Sladek, Sladek, and Keer (2000); Han and Atluri (2003b); Sellountos and Polyzos (2005b); Bodin, Ma, Xin, and Krishnaswami (2006)], in thermoelasticity [Sladek, Sladek, and Atluri (2001)], in micropolar elasticity [Sladek and Sladek (2003)], in 2D elastodynamic problems [Sladek, Sladek, and Keer (2003); Sladek, Sladek, and Mang (2003); Sellountos and Polyzos (2003, 2005a)] and in 3D heat conduction and elasticity with geometry axisymmetry [Sladek, Sladek, Krivacek, and Zhang (2003); Vavourakis and Polyzos (2006)]. Recently,

the two papers of [Atluri, Han, and Rajendran (2004); Vavourakis and Polyzos (2007)] in two-dimensional linear elasticity, present mixed-type formulations in the MLPG and LBIE methods, respectively.

In this paper, a Local Hypersingular Boundary Integral Equation (LHBIE) method is proposed for elastostatics in two dimensions. The local form of the boundary integral representations, taken from the BEM, of displacements and stresses is utilized. The analyzed domain is discretized by a distribution of nodes. From this set of nodes it is defined a “background” mesh of triangular cells. The local domain of a node is considered to be the union of its neighbourhood triangles. In this subdomain, all local boundary integrals are evaluated. Thus, a discretized system of equilibrium equations is obtained. Some examples in two-dimensional elastostatics are solved, in order to validate and verify the proposed LHBIE method. The numerical results obtained by the LHBIE method demonstrate that the accuracy and stability of this formulation is as good as that of the BEM.

2 The Local Hypersingular Boundary Integral Equation method

In this section, a thorough presentation of the Local Hypersingular Boundary Integral Equation (LHBIE) method in elastostatics for the special case of two dimensions is given. In the first subsection, the integral equations of displacements and stresses are given and the local form of the afore-mentioned integral equations is produced. Given that the elastic body is discretized with a distribution of nodes, a set of discrete equations that form the final linear system is derived. In the second subsection, the numerical implementation of the LHBIE method is discussed and some comments regarding critical numerical issues on the proposed methodology are made.

2.1 The LHBIE method in two-dimensional elastostatics

Consider an elastic body of volume Ω , bounded by surface Γ , as seen in Fig. 1. Equilibrium at a point $\mathbf{x} \in \Omega$ of the continuous medium is described by the following Navier-Cauchy partial differential equation [Timoshenko and Goodier (1970)]:

$$\mu u_{i,jj}(\mathbf{x}) + (\lambda + \mu) u_{j,ji}(\mathbf{x}) = f_i(\mathbf{x}), \quad i, j = 1, 2, \quad (1)$$

where λ, μ are the Lamè elastic constants, u_i the displacement vector field and f_i the body forces (i.e. gravity or centrifugal load). For the present analysis the influence of vector f_i is neglected.

The boundary-value problem is fully described by the set of boundary conditions below

$$u_i(\mathbf{x}) = \bar{u}_i, \quad \forall \mathbf{x} \in \Gamma_{\mathbf{u}}, \quad (2a)$$

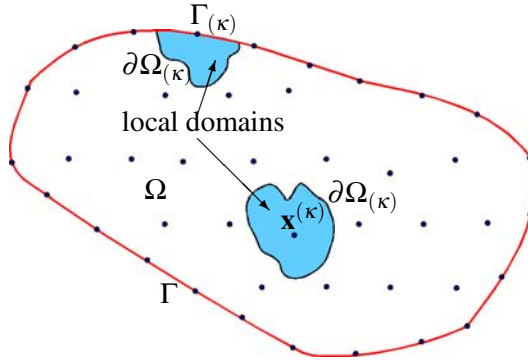


Figure 1: Elastic domain Ω bounded by surface Γ having scattered nodal points inside and on its boundary.

$$t_i(\mathbf{x}) = \bar{t}_i, \quad \forall \mathbf{x} \in \Gamma_t, \quad (2b)$$

where $\Gamma = \Gamma_u \cup \Gamma_t$, and \bar{u}_i, \bar{t}_i represent the prescribed displacement and traction vectors.

The integral representation of the above described problem at a discrete source point $\mathbf{x}^{(\kappa)} \in \Omega$ is [Banerjee (1994); Brebbia and Dominguez (1998); Guiggiani, Krishnasamy, Rudolphi, and Rizzo (1992)]

$$\alpha_{ij}(\mathbf{x}^{(\kappa)}) u_j(\mathbf{x}^{(\kappa)}) = \lim_{V_\varepsilon \rightarrow 0} \left\{ \int_{\Gamma - \Gamma^{(\kappa)\varepsilon}} \left[u_{ij}^*(\mathbf{x}^{(\kappa)}, \mathbf{y}) t_j(\mathbf{y}) - t_{ij}^*(\mathbf{x}^{(\kappa)}, \mathbf{y}) u_j(\mathbf{y}) \right] dS_{\mathbf{y}} \right\}. \quad (3)$$

Array α_{ij} is described in Eq. (25) of the Appendix, and the fundamental solution kernels u_{ij}^*, t_{ij}^* are given in Appendix A. The presence of the limit is due to the singular behaviour of the kernels as field point \mathbf{y} approaches the singular source point. If someone takes an arbitrary small subdomain V_ε around $\mathbf{x}^{(\kappa)}$ (see Fig. 2), then the second Green's identity can be written and after some algebra the final form of the boundary integral Eq. (3) can be produced.

In the special case when source point $\mathbf{x}^{(\kappa)}$ lies on a smooth boundary or it is located inside the analyzed body then Eq. (3) takes the form

$$\alpha_{ij}(\mathbf{x}^{(\kappa)}) u_j(\mathbf{x}^{(\kappa)}) = \int_{\Gamma} \left[u_{ij}^*(\mathbf{x}^{(\kappa)}, \mathbf{y}) t_j(\mathbf{y}) - t_{ij}^*(\mathbf{x}^{(\kappa)}, \mathbf{y}) u_j(\mathbf{y}) \right] dS_{\mathbf{y}}, \quad (4)$$

and the free-term coefficient α_{ij} is calculated analytically, where for smooth boundary points it is equal to $\delta_{ij}/2$ and δ_{ij} for internal ones.

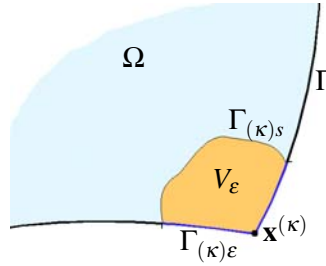


Figure 2: Boundaries of exclusion for a singular boundary point $\mathbf{x}^{(\kappa)}$ by a vanishing neighbourhood V_ϵ .

Taking the gradient on Eq. (3) and applying successively Hooke’s law, then it can be derived the corresponding hypersingular boundary integral representation of stresses

$$a_{ijln}(\mathbf{x}^{(\kappa)}) \sigma_{ln}(\mathbf{x}^{(\kappa)}) + b_{ijk}(\mathbf{x}^{(\kappa)}) u_k(\mathbf{x}^{(\kappa)}) = \lim_{V_\epsilon \rightarrow 0} \left\{ \int_{\Gamma - \Gamma^{(\kappa)}_\epsilon} \left[u_{ijk}^*(\mathbf{x}^{(\kappa)}, \mathbf{y}) t_k(\mathbf{y}) - t_{ijk}^*(\mathbf{x}^{(\kappa)}, \mathbf{y}) u_k(\mathbf{y}) \right] dS_{\mathbf{y}} \right\}, \quad (5)$$

where σ_{ln} is the stress tensor. The third-order tensors u_{ijk}^*, t_{ijk}^* are given in Appendix A, as well as the expressions for the forth- and third-order tensors of the free-term coefficients can be found in Appendix B.

However, it is interesting to refer to the works [Okada, Rajiyah, and Atluri (1989); Han and Atluri (2003a,b, 2007)], where a direct derivation of the strongly-singular boundary integral equations of displacement gradients is adopted. In this paper, only the classical hypersingular boundary integral Eq. (5) of stresses is taken into account.

Given that the stress tensor is symmetric for isotropic linear elastic media ($\sigma_{12} = \sigma_{21}$), then someone can make use of a new stress vector: $\tau = \{\sigma_{11} \ \sigma_{22} \ \sigma_{12}\}^T$. Subsequently, in the special case of internal nodes or nodes lying on a smooth boundary, Eq. (5) can take a new form

$$c_{ij}(\mathbf{x}^{(\kappa)}) \tau_j(\mathbf{x}^{(\kappa)}) = \int_{\Gamma} \left[U_{ij}^*(\mathbf{x}^{(\kappa)}, \mathbf{y}) t_j(\mathbf{y}) - T_{ij}^*(\mathbf{x}^{(\kappa)}, \mathbf{y}) u_j(\mathbf{y}) \right] dS_{\mathbf{y}}, \quad (6)$$

where the 3×3 array c_{ij} takes the same values like α_{ij} and the second free-term of

Eq. (5) vanishes. The new kernels U_{ij}^* and T_{ij}^* are arrays having the form

$$U_{ij}^* = \begin{bmatrix} u_{111}^* & u_{112}^* \\ u_{221}^* & u_{222}^* \\ u_{121}^* & u_{122}^* \end{bmatrix} \quad \text{and} \quad T_{ij}^* = \begin{bmatrix} t_{111}^* & t_{112}^* \\ t_{221}^* & t_{222}^* \\ t_{121}^* & t_{122}^* \end{bmatrix} \quad (7)$$

As it is known from the literature, both boundary integral equations (4) and (6) become singular and hypersingular, respectively, only when the field point \mathbf{y} gets close to the source point $\mathbf{x}^{(\kappa)}$. Therefore someone can write both integral representations into a local form

$$\alpha_{ij}(\mathbf{x}^{(\kappa)}) u_j(\mathbf{x}^{(\kappa)}) + \int_{\Gamma_{(\kappa)} \cup \partial\Omega_{(\kappa)}} t_{ij}^*(\mathbf{x}^{(\kappa)}, \mathbf{y}) u_j(\mathbf{y}) dS_{\mathbf{y}} = \int_{\Gamma_{(\kappa)} \cup \partial\Omega_{(\kappa)}} u_{ij}^*(\mathbf{x}^{(\kappa)}, \mathbf{y}) t_j(\mathbf{y}) dS_{\mathbf{y}}, \quad (8)$$

$$c_{ij}(\mathbf{x}^{(\kappa)}) \tau_j(\mathbf{x}^{(\kappa)}) + \int_{\Gamma_{(\kappa)} \cup \partial\Omega_{(\kappa)}} T_{ij}^*(\mathbf{x}^{(\kappa)}, \mathbf{y}) u_j(\mathbf{y}) dS_{\mathbf{y}} = \int_{\Gamma_{(\kappa)} \cup \partial\Omega_{(\kappa)}} U_{ij}^*(\mathbf{x}^{(\kappa)}, \mathbf{y}) t_j(\mathbf{y}) dS_{\mathbf{y}}, \quad (9)$$

where $\partial\Omega_{(\kappa)}$ and $\Gamma_{(\kappa)}$ are illustrated in Fig. 1.

The surface traction vector t_j is associated with the stress vector τ_k through the relation

$$t_j(\mathbf{y}) = N_{jk}(\mathbf{y}) \tau_k(\mathbf{y}) = \begin{bmatrix} \hat{n}_1 & 0 & \hat{n}_2 \\ 0 & \hat{n}_2 & \hat{n}_1 \end{bmatrix} \tau_k(\mathbf{y}), \quad (10)$$

and \hat{n}_i is the outward unit normal vector component at $\mathbf{y} \in \partial\Omega_{(\kappa)}$.

Replacing the traction vector of the internal local-boundary integrals over $\partial\Omega_{(\kappa)}$ via Eq. (10) in the previous set of integral equations, then someone can write

$$\alpha_{ij}(\mathbf{x}^{(\kappa)}) u_j(\mathbf{x}^{(\kappa)}) + \int_{\Gamma_{(\kappa)} \cup \partial\Omega_{(\kappa)}} t_{ij}^*(\mathbf{x}^{(\kappa)}, \mathbf{y}) u_j(\mathbf{y}) dS_{\mathbf{y}} = \int_{\Gamma_{(\kappa)}} u_{ij}^*(\mathbf{x}^{(\kappa)}, \mathbf{y}) t_j(\mathbf{y}) dS_{\mathbf{y}} + \int_{\partial\Omega_{(\kappa)}} u_{ij}^*(\mathbf{x}^{(\kappa)}, \mathbf{y}) N_{jk}(\mathbf{y}) \tau_k(\mathbf{y}) dS_{\mathbf{y}}, \quad (11)$$

$$c_{ij}(\mathbf{x}^{(\kappa)}) \tau_j(\mathbf{x}^{(\kappa)}) + \int_{\Gamma_{(\kappa)} \cup \partial\Omega_{(\kappa)}} T_{ij}^*(\mathbf{x}^{(\kappa)}, \mathbf{y}) u_j(\mathbf{y}) dS_{\mathbf{y}} =$$

$$\int_{\Gamma^{(\kappa)}} U_{ij}^* (\mathbf{x}^{(\kappa)}, \mathbf{y}) t_j (\mathbf{y}) dS_{\mathbf{y}} + \int_{\partial\Omega^{(\kappa)}} U_{ij}^* (\mathbf{x}^{(\kappa)}, \mathbf{y}) N_{jk} (\mathbf{y}) \tau_k (\mathbf{y}) dS_{\mathbf{y}}. \quad (12)$$

The above mentioned two-dimensional elastostatic body has been discretized so far by placing arbitrarily nodes in the domain. However from the specified set of nodes someone can construct a “background” mesh of triangles, as seen in Fig. 3. It is easy to notice from this figure the local domains of each node (shaded areas), which are formed by the union of triangles that node $\mathbf{x}^{(\kappa)}$ belongs. In Fig. 3, the local boundaries $\Gamma^{(\kappa)}$ and $\partial\Omega^{(\kappa)}$ for boundary and internal nodal points $\mathbf{x}^{(\kappa)}$ are depicted, which have a poly-line shape.

In the present formulation no Moving Least Squares approximation or Radial Basis Functions interpolation scheme is employed. However, each side of the aforementioned triangles is treated as a common one-dimensional element. The nodes that define this element is the pair of vertices of the triangle on its corresponding side.

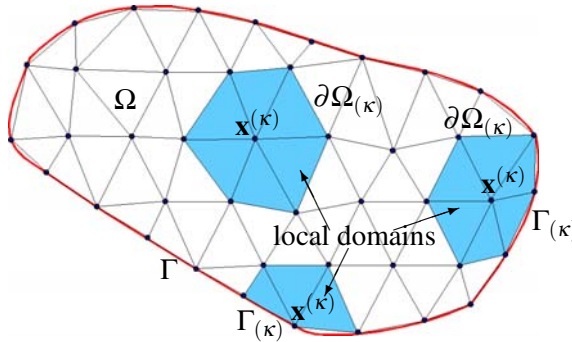


Figure 3: Discretized elastic domain with boundary and internal nodes, and the corresponding underlying triangles. The local boundaries $\partial\Omega^{(\kappa)}$ and $\Gamma^{(\kappa)}$ of the respective points $\mathbf{x}^{(\kappa)}$ are shown in detail.

Thus, for the interpolation of the unknown field variables the well-known shape functions of the line elements are utilized [Brebbia and Dominguez (1998)]. In addition, the displacement and stress vector are treated as independent variables. The interpolation relations are the ones below

$$u_j = \Phi_{jl} \check{u}_l, \quad (13a)$$

$$t_j = \Phi_{jl} \check{t}_l, \quad (13b)$$

$$\tau_k = \Theta_{kn} \check{\tau}_n, \quad (13c)$$

where Φ_{jl} for a two-node element is a 2×4 matrix, and Θ_{kn} is a 3×6 matrix, both arrays containing the same interpolation functions of the element [Brebbia and

Dominguez (1998)]. Vectors \check{u}_l , \check{t}_l and $\check{\tau}_n$ represent the nodal values of the element of the respective fields.

Inserting interpolation Eqs. (13) into integral Eqs. (11) and (12), then someone can obtain

$$\alpha_{ij}(\mathbf{x}^{(k)}) u_j(\mathbf{x}^{(k)}) + \int_{\Gamma_{(k)} \cup \partial\Omega_{(k)}} t_{ij}^*(\mathbf{x}^{(k)}, \mathbf{y}) \Phi_{jl} dS_{\mathbf{y}} \check{u}_l = \int_{\Gamma_{(k)}} u_{ij}^*(\mathbf{x}^{(k)}, \mathbf{y}) \Phi_{jl} dS_{\mathbf{y}} \check{t}_l + \int_{\partial\Omega_{(k)}} u_{ij}^*(\mathbf{x}^{(k)}, \mathbf{y}) N_{jk}(\mathbf{y}) \Theta_{kn} dS_{\mathbf{y}} \check{\tau}_n, \quad (14)$$

and

$$c_{ij}(\mathbf{x}^{(k)}) \tau_j(\mathbf{x}^{(k)}) + \int_{\Gamma_{(k)} \cup \partial\Omega_{(k)}} T_{ij}^*(\mathbf{x}^{(k)}, \mathbf{y}) \Phi_{jl} dS_{\mathbf{y}} \check{u}_l = \int_{\Gamma_{(k)}} U_{ij}^*(\mathbf{x}^{(k)}, \mathbf{y}) \Phi_{jl} dS_{\mathbf{y}} \check{t}_l + \int_{\partial\Omega_{(k)}} U_{ij}^*(\mathbf{x}^{(k)}, \mathbf{y}) N_{jk}(\mathbf{y}) \Theta_{kn} dS_{\mathbf{y}} \check{\tau}_n. \quad (15)$$

After the numerical evaluation of all integrals, a set of linear equations is deduced

$$H_{ij} \check{u}_j = G_{ik} \check{t}_k + S_{il} \check{\tau}_l, \quad (16)$$

where matrix H_{ij} contains the left-hand side boundary integrals of Eqs. (14), (15) and the free-term of Eq. (14). Matrix G_{ik} contains the right-hand side boundary integrals where the traction vector \check{t}_k is unknown. Matrix S_{il} contains the corresponding boundary integrals where the stress vector $\check{\tau}_l$ is unknown, plus the free-term of Eq. (15). The size of the above matrices varies according to the neighbourhood nodal points of $\mathbf{x}^{(k)}$. In the general case when $\mathbf{x}^{(k)}$ has N_e neighbourhood nodes then arrays H_{ij} , G_{ik} have size equal to $5 \times 2(N_e + 1)$ and S_{il} has size equal to $5 \times 3(N_e + 1)$.

Collocating for all N nodes of the mesh, a system of N linear equations is created in the form of Eq. (16). The next step is to insert the Boundary Conditions (BCs) of Eq. (2) in the set of equations (16). By definition, the interpolation functions that are utilized in this formulation possess the Kronecker delta-function property. Therefore, essential BCs can be imposed directly, as in BEM and FEM. For boundary nodes whose tractions are prescribed, BCs are inserted straightforwardly in vector \check{t}_k ($\equiv \check{t}_k$). On the other hand, when displacements are prescribed, BCs are inserted accordingly in vector \check{u}_j ($\equiv \check{u}_j$) and the corresponding traction components are replaced by stresses through Eq. (10). Thus, the only unknown quantities are displacement or tractions and stresses for boundary nodes, and for internal nodes the unknown values are displacements and stresses. After splitting known from unknown nodal values, then someone can be led to a final system of equations

$$A_{ij} \chi_j = \beta_i, \quad (17)$$

where matrix A_{ij} is a $5N \times 5N$ banded matrix and the right-hand side vector β_i contains the local boundary integrals with prescribed boundary conditions.

2.2 Numerical Implementation

As reported in Section 1, the two-dimensional elastic region is discretized by placing arbitrarily boundary and internal nodes. The pattern of the distribution of nodes, as it will be shown in the following numerical examples, is not particular. Someone can adopt a uniform or a non-uniform distribution of nodes. Given the set of nodes and an explicit definition of the boundary that describes the surface geometry (see Fig. 1), a triangular “background” mesh is produced (see Fig. 3). In Subsection 2.1 it is stated that these triangles do not play an important role, by means of interpolating the field values. They only give information about the shape and size of the local domain of integration ($\partial\Omega_{(\kappa)}$ and $\Gamma_{(\kappa)}$) of a source point $\mathbf{x}^{(\kappa)}$. However, as depicted in Fig. 4, the size of the local domain can be chosen at will. In this paper, the local domain is primarily the union of triangles that contain the node of interest (see Fig. 4(a)). In case when an extended size of the local domain is desirable then some more neighboring triangles are taken into account too. From now on the local domain described by the stencils of Figs. 4(a), 4(b), 4(c) will be referred as Type-1, Type-2 and Type-3, respectively. Obviously, if the size of the local domain extends in a way that it covers the whole domain Ω of the body then this method is identical to the BEM.

In the above-mentioned local boundary integral Eqs. (11), (12) all boundary nodes are assumed to lie on a smooth boundary Γ , which leads to a direct adoption of free-term coefficient matrices α_{ij} and c_{ij} , respectively, equal to $\delta_{ij}/2$. In the framework of the present paper, it was tested firstly to make use of corner nodes in the numerical analysis. Thus, the numerical evaluation of the free-term coefficient matrices, as reported in [Guiggiani (1995)], was investigated. After solving a few elastostatic benchmark problems, the results were not that satisfactory. The numerical results showed low accuracy levels, due to the hypersingularity of the kernels involved. The second step, was to simply displace corner nodes from the local discontinuity of the geometry (see Fig. 5), as in the conventional BEM [Banerjee (1994)]. Although this measure increases the total number of nodes in the mesh, the obtained numerical results were of very good quality, as it will be demonstrated in the next section.

Major role in the accuracy and stability of the BEM and the proposed LHBIE method is the numerical evaluation of singular and hypersingular boundary integrals. For the evaluation of these integrals someone can reference papers [Guiggiani, Krishnasamy, Rudolphi, and Rizzo (1992); Guiggiani (1994, 1995); Frangi and Guiggiani (2000); Sladek, Sladek, and Keer (2000)]. Especially in papers

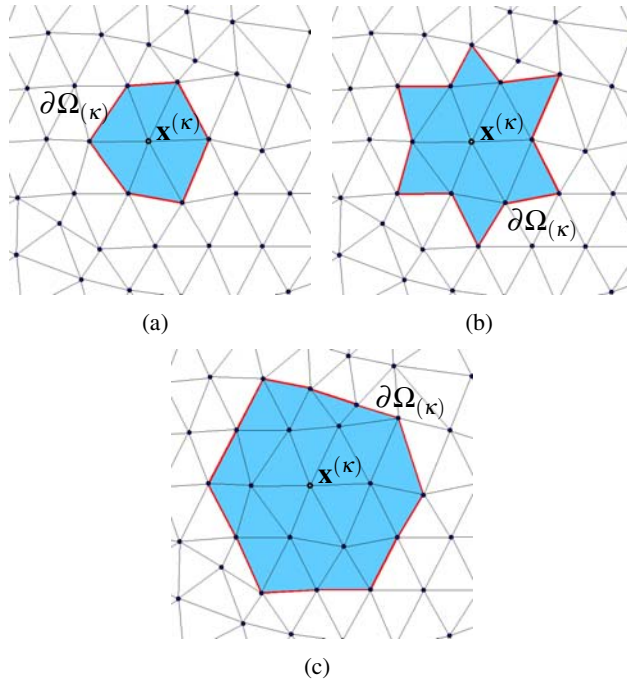


Figure 4: Local domain of source point $\mathbf{x}^{(\kappa)}$ defined by a stencil of (a) six, (b) twelve and (c) eighteen neighboring nodes, where the corresponding “background” triangular cells are shown in detail.

[Guiggiani, Krishnasamy, Rudolphi, and Rizzo (1992); Guiggiani (1994)] a direct approach for the numerical calculation of singular and hypersingular boundary integrals is described. For the present analysis only eight Gauss-Legendre quadrature points were needed for the evaluation of integrals on Γ and $\Gamma_{(\kappa)}$. Furthermore, the number of quadrature points required for the local boundary integrals on $\partial\Omega_{(\kappa)}$ to converge was defined by the explicit rule given in [Bu (1997)].

As it will be seen in the next section, the computational time consumed by the BEM is much higher than that of the LHBIE method. It should be noted here that the time consumed by the solver to solve the final system of Eq. (17) is lower in the BEM than in the LHBIE method. For example, if someone assumes that the elastic body is discretized with N_b boundary nodes and N_i internal ones then matrix A_{ij} has size equal to $2N_b \times 2N_b$ in the conventional BEM. On the other hand, the size of the same matrix in the LHBIE method is $5(N_b + N_i) \times 5(N_b + N_i)$, which is much higher than that of BEM. However for the assembly of A_{ij} in the BEM only the boundary nodes take part and the field variables of the internal nodes

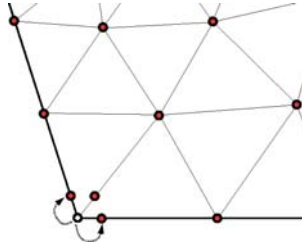


Figure 5: Detail on corner node that has been tripled and displaced from the geometrical discontinuity.

are obtained by solving Eq. (16) in post-process. In the LHBIE method instead, as stated before, all nodes take part in the derivation of matrix A_{ij} and the field variables are obtained straightforwardly. The main reason why the BEM consumes more computational time than the proposed methodology is that the evaluation of boundary integrals on Γ in the former method is computationally cumbersome. The LHBIE method however evaluates boundary integrals only on the local boundary $\Gamma_{(\kappa)} \cup \partial\Omega_{(\kappa)}$, which is much smaller than that of the global boundary Γ . In addition, in case when both methods end up to comparable degrees-of-freedom in the final system, the BEM forms a fully-populated matrix A_{ij} , while the LHBIE forms a banded matrix. Thus, faster solution of the final system can be achieved through the proposed methodology.

In the framework of this paper, the well-established BEM is implemented in order to compare the numerical results obtained by the LHBIE methodology. Details on how the BEM formulation is implemented can be found in the comprehensive books [Banerjee (1994); Brebbia and Dominguez (1998)]. In brief, for all boundary nodes integral Eq. (4) is collocated and a set of linear equations is produced. Inserting in this set of equations boundary conditions and splitting known from unknown variables a final linear system is produced (same as in Eq. (17)). Only unknown boundary displacements or/and tractions are evaluated numerically. Then for all boundary and internal nodes the corresponding boundary integral equation of stresses (see Eq. (6)) is solved in post-process so as to obtain the stress field.

3 Numerical Examples

In this section three two-dimensional elastostatic problems are solved, in order to validate the Local Hypersingular Boundary Integral Equation method. Through these examples, the accuracy, the convergence and stability of the proposed methodology is demonstrated as well.

The LHBIE method is coded in the C++ programming language. The same computer program is also designed to implement the Boundary Element Method. The triangulations are obtained with the aid of Shewchuk's program "Triangle" [Shewchuk (1996, 2002)] written in ANSI-C. All numerical simulations are performed on a Linux platform having an AMD Turion 64 ML-34 processor and 1GB RAM.

In order to estimate the numerical results accuracy and convergence, the displacement relative error L_2 norm is evaluated, i.e.

$$L_{2\mathbf{u}} = \frac{1}{N} \sqrt{\frac{\sum_{i=1}^N \|\check{\mathbf{u}}^{(i)} - \mathbf{u}^{(i)}\|^2}{\sum_{j=1}^N \|\check{\mathbf{u}}^{(j)}\|^2}}, \quad (18)$$

where N is the total number of nodes of the analyzed body, $\check{\mathbf{u}}^{(i)}$ is the analytic results' displacement vector of node i and $\mathbf{u}^{(i)}$ is the respective numeric results' vector of the same node. The corresponding $L_{2\tau}$ relative error norm of the stress vector τ has the same form like the one of Eq. (18) for the displacement vector.

3.1 Plate under uniform uniaxial load

Consider a $2\text{m} \times 2\text{m}$ metallic plate having elastic properties: $E = 200\text{GPa}$ Young modulus and $\nu = 0.29$ Poisson ratio. This plate has been subject to uniform horizontal load $P = 10\text{MPa}$ and plane-stress conditions are assumed. Due to symmetry only the upper right quadrant of the plate is analyzed. Thus, symmetry conditions are applied to both the right and the bottom edge of the plate ($u_1 = 0$ for $x_1 = 0$ and $u_2 = 0$ for $x_2 = 0$ respectively). The quarter plate has been discretized by distributing evenly 25, 36, 49 and 64 nodes, as depicted in Fig. 6. For the BEM the boundary of the square plate has been discretized with two-node linear elements.

This problem has been solved through the BEM and the LHBIE method for all mesh distributions. In addition, the proposed methodology is also tested for three types of the local domain. From now on we will denote LHBIE T-1 to the LHBIE method with a local domain of size as illustrated in Fig. 4(a), the LHBIE T-2 corresponds to a local domain of Fig. 4(b) and LHBIE T-3 to that of Fig. 4(c). Furthermore, the accuracy and efficiency of the proposed methodology compared with the most common Meshless Local Petrov-Galerkin (MLPG) and Local Boundary Integral Equation (LBIE) formulations is examined. For these meshless methodologies, a linear MLS approximation basis with a Gaussian weight function is utilized, and a support domain equal to $1.43 \times \delta$ for all nodes is set, where δ the mean distance of two consecutive nodes (for details refer to paper [Zhu, Zhang, and Atluri (1998)]).

The displacement relative error norms obtained by the BEM, the LHBIE method, the MLPG-1, MLPG-5 and MLPG-6 formulations [Atluri and Shen (2002)], the

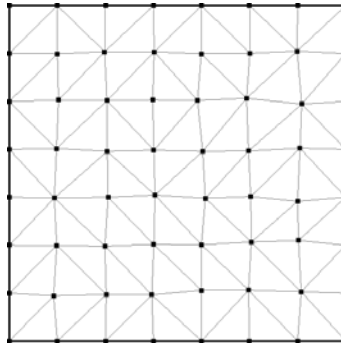


Figure 6: Distribution of 64 nodes on the quarter square plate and the underlying triangular cells.

MLPG(LBIE) [Sellountos and Polyzos (2005b)] and the MLPG4(LBIE) formulation [Vavourakis and Polyzos (2008)] are depicted in Fig. 7. Symbol h in Fig. 7 is a mesh density factor that is defined by the mean minimum distance of nodes of the mesh, whereas the lower its value the denser the mesh is. From this figure it can be noticed that the newly proposed LHBIE method produces results of very high accuracy compared to those of BEM and MLPG-5, and even better to those of the LBIE formulations and MLPG-1 and MLPG-6. However it should be noted here, as reported in [Atluri, Kim, and Cho (1999); Vavourakis, Sellountos, and Polyzos (2006)], that the MLPG is sensitive to the support domain size as well as to the weight function utilized in the MLS approximation scheme. Thus, the results depicted in Fig. 7 for the MLPG methodologies are not fully representative. On the other hand, from Fig. 7 it is shown that the LHBIE method is less sensitive to the local domain decision. The same conclusion will be drawn from the numerical examples that follow.

3.2 Kirsch benchmark problem

The next benchmark problem that is to be solved is of a 2m long square plate having a circular hole on its center. The radius of the hole is equal to $R = 0.15\text{m}$. As in Subsection 3.1, the plate is subjected to a uniform tensile load of $P = 10\text{MPa}$ and plane-stress conditions are assumed. This problem is known in the literature as the Kirsch problem. In book [Timoshenko and Goodier (1970)] someone can find the analytical solutions to this problem. For this case various mesh densities were assumed: 410, 575, 801 and 1025 nodes; evenly distributed on the right quadrant of the perforated plate (see Fig. 8).

After numerically solving this benchmark problem the obtained results are com-

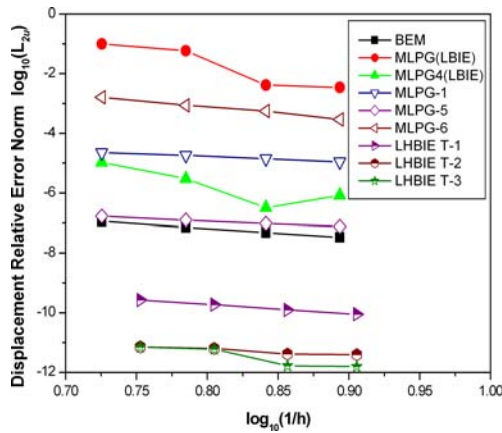


Figure 7: Relative error norms of displacements for the linear patch test benchmark problem obtained by various numerical methods.

Table 1: Convergence rates on numerical solutions of displacement and stress field by the BEM and the LHBIE method on the Kirsch benchmark problem.

	displacements	stresses
BEM	2.14	2.58
LHBIE T-1	2.15	3.02
LHBIE T-2	2.19	2.89
LHBIE T-3	2.05	1.10

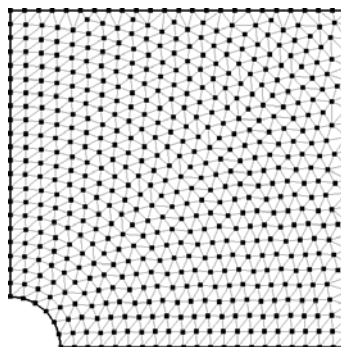


Figure 8: Uniform distribution of 575 nodes on a quarter of the plate for the Kirsch benchmark problem.

pared to the corresponding analytical ones. The relative error norm of displacements and stresses is calculated through Eq. (18). In Fig. 9 the L_2 norms for both methods and for all four mesh densities are depicted. From Fig. 9(a) it can be drawn the conclusion that the BEM and the LHBIE method produce almost the same accurate results for the displacement field and they both converge in the same manner. In Fig. 9(b) it can be noted that the BEM produces better solution of the stress field compared with the LHBIE, but the latter method seems to converge faster than the former.

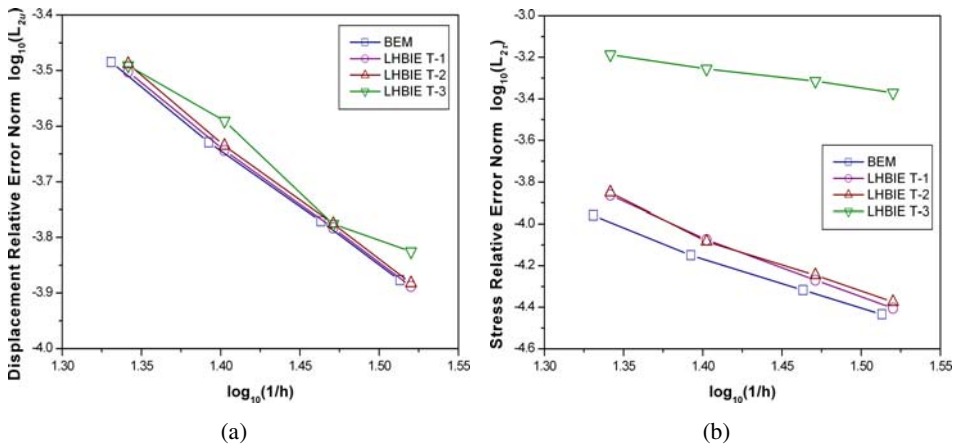


Figure 9: Relative error norms of (a) displacements and (b) stresses for the Kirsch benchmark problem.

In Table 1 it is shown the convergence rates of displacements and stresses of both numerical methods. From that table it can be drawn the conclusion that the proposed LHBIE method has almost the same convergence rate (second order) with the BEM in terms of the displacement field, and significantly better in terms of the stress field (almost third order). It can be also seen from that table that if the local domain is chosen to be of the third type (see Fig. 4(c)) then the convergence rates tend to fall.

Table 2: Computational time consumed by various numerical methods for solving the Kirsch benchmark problem for all mesh densities.

# of Nodes	BEM	BEM*	MLPG-1	MLPG-5	MLPG-6	MLPG(LBIE)	MLPG4(LBIE)	LHBIE T-1	LHBIE T-2	LHBIE T-3
410	715s	134s	602s	40s	578s	96s	160s	71s	73s	75s
575	1452s	285s	840s	62s	801s	129s	252s	146s	151s	152s
801	2835s	543s	1248s	101s	1196s	180s	436s	286s	289s	296s
1025	5492s	855s	1636s	146s	1570s	230s	648s	507s	511s	516s

In Table 2 it is shown the computational time consumed by the BEM and the LHBIE method to solve the Kirsch benchmark problem for various mesh densities. On the third column of Table 2 it is shown the computational time consumed by the BEM, where internal points were not taken into account in the analysis and the numerical evaluation of stresses is omitted. In addition, it is shown the computational time consumed by the MLPG-1, MLPG-5 and MLPG-6 formulations, the MLPG(LBIE) and MLPG4(LBIE) methodologies. As explained in Subsection 2.2, the reason why it takes more time for the BEM to perform its analysis is the numerical evaluation of the integrals on the global boundary Γ . On the other hand, the LHBIE evaluates integrals only on the local boundary $\Gamma_{(\kappa)} \cup \partial\Omega_{(\kappa)}$ of a node, which is significantly smaller to that of Γ . In addition, formulations MLPG-1 and MLPG-6 consume excessive computational time due to the numerical evaluation of volume integrals. The fastest numerical method of all seems to be the MLPG-5, where the Heaviside step function is utilized as a test function over the computational domain and only regular boundary integrals are evaluated.

3.3 Perforated plate under tension

The final numerical example is that of a plate that has five circular holes, as shown in Fig. 10(a). The same material properties and magnitude of the tension load is applied, like in the benchmark problem of Subsection 3.1. Due to symmetry of the geometry and the boundary conditions only the upper right quadrant is analyzed, as seen in Fig. 10(b). A non-uniform distribution of nodes is adopted, where a density of 364, 445, 574 and 738 nodes is utilized on the quarter perforated plate.

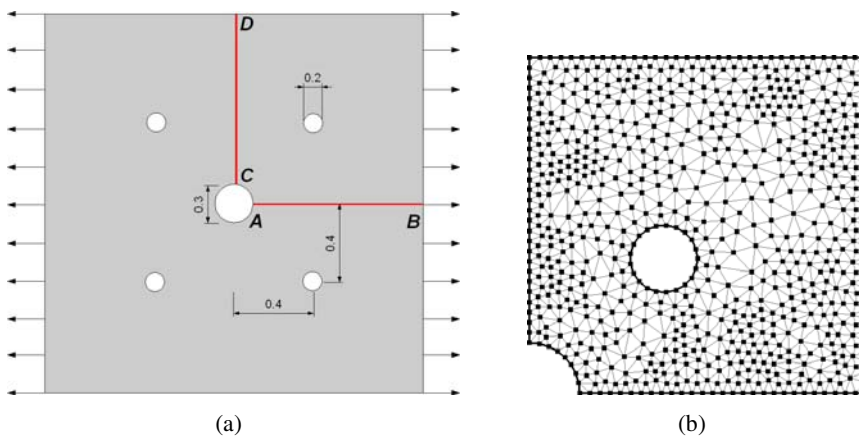


Figure 10: (a) Geometry of the perforated plate, (b) a non-uniform distribution of 738 nodes and “background” triangular cells.

Due to the lack of an analytical solution to this example, the obtained numerical results of the LHBIE method are compared with the corresponding ones of the BEM. In Figs. 11, 12 it is depicted the numerical results' comparison of both methods for various meshes at lines CD and AB (see Fig. 10(a)), respectively. From these figures someone can notice that there is good agreement between those numerical methods on the displacement field (see Figs. 11(a) and 12(a)) and on the evaluation of the σ_{11} , σ_{12} stresses (see Figs. 12(b), 12(c) and Figs. 11(b), 11(c)). On the other hand, on the σ_{22} stress field the numerical results between the BEM and the LHBIE method seem not to coincide. One reason why this happens is that the σ_{22} stress field is approximately two orders lower than the corresponding maximum value of the σ_{11} one.

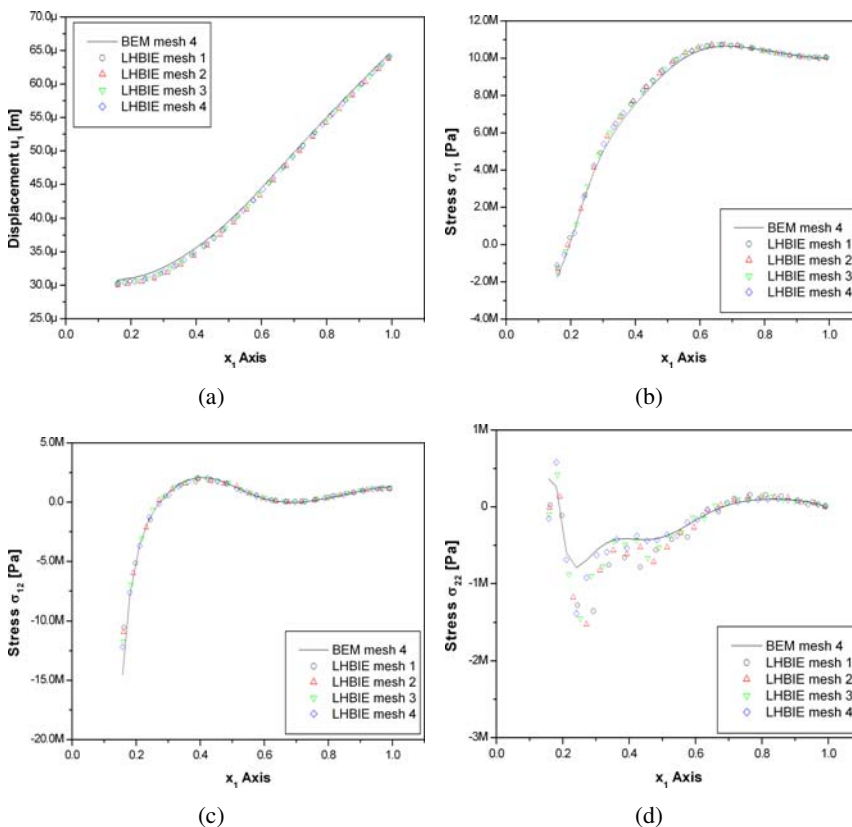


Figure 11: Comparison of numerical results obtained by the BEM and the LHBIE method at line AB for the perforated plate problem.

For demonstration purposes, in Figs. 13 and 14 the contour plots of the displace-

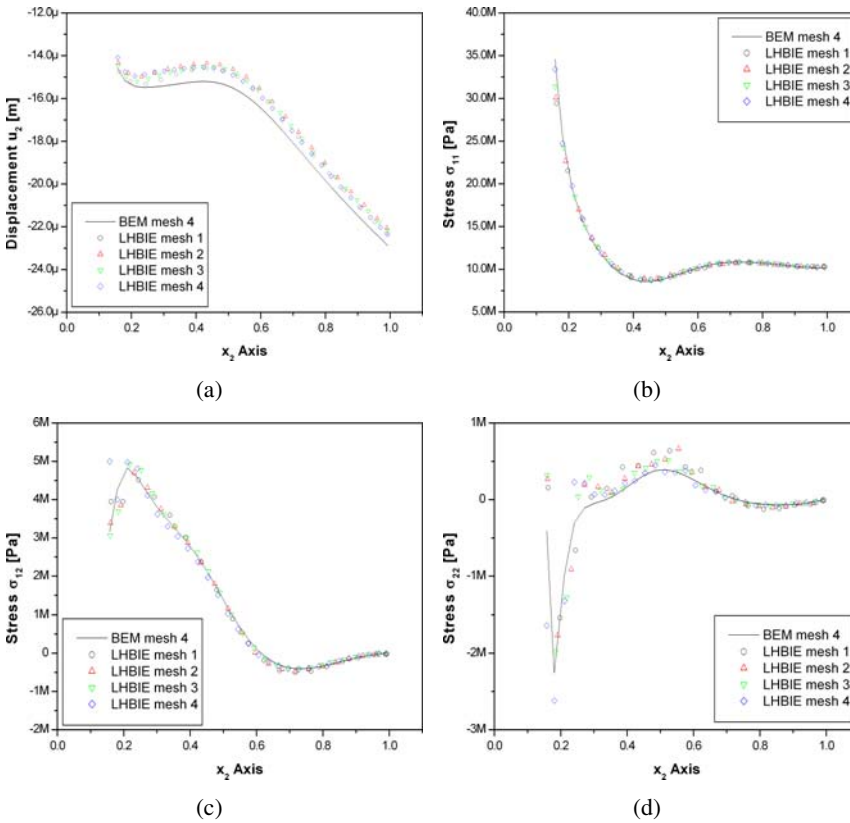


Figure 12: Comparison of numerical results obtained by the BEM and the LHBIE method at line CD for the perforated plate problem.

ment and stress field are depicted. The numerical results were obtained by the LHBIE method, using a 738-node mesh (see Fig. 10(b)) and a Type-1 local domain stencil.

In addition in Table 3 it is shown the computational time consumed by the conventional boundary elements and the proposed meshless methodology. Once again it can be noted that the BEM takes significantly more computational time than the LHBIE method to accomplish its numerical analysis.

4 Remarks

The advantages and disadvantages of the LHBIE methodology, compared to the conventional Boundary Elements Method and most Meshless Local Petrov-Galerkin methods can be summarized as follows:

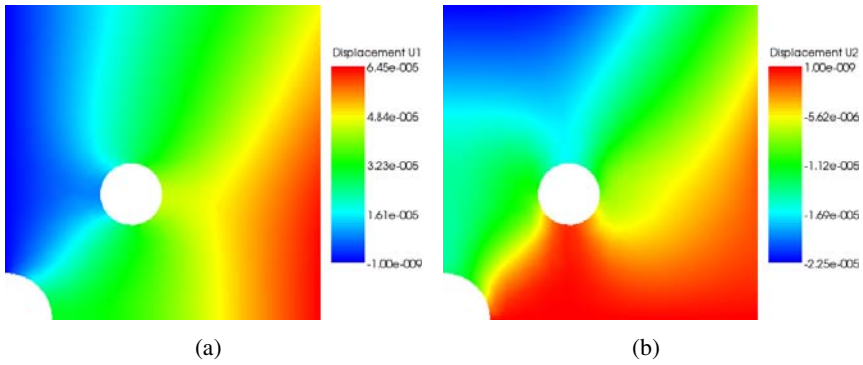


Figure 13: Contour plots of the displacement field obtained by the LHBIE method for the perforated plate problem.

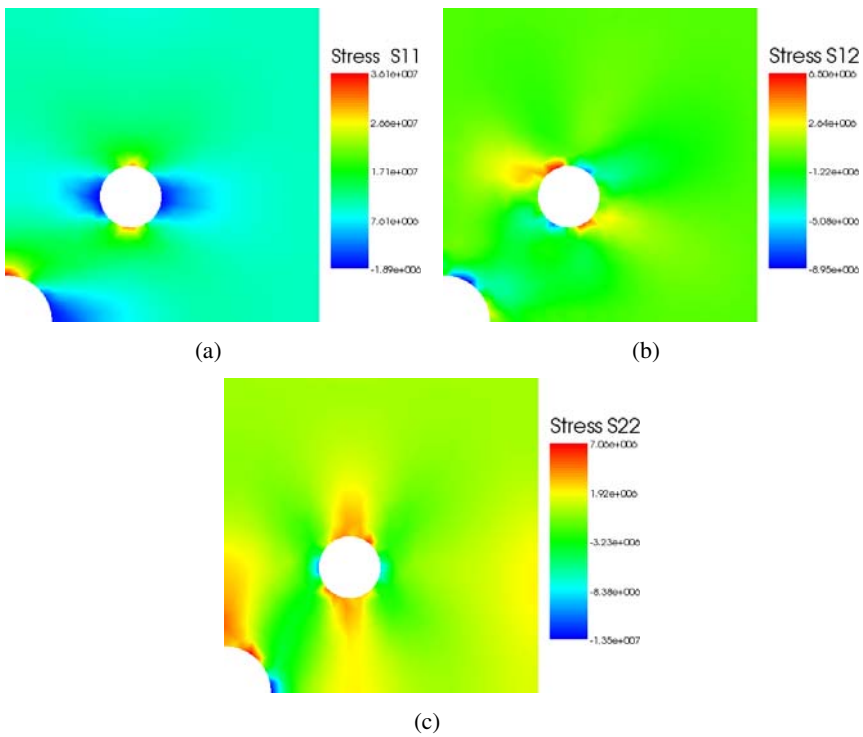


Figure 14: Contour plots of the stress field obtained by the LHBIE method for the perforated plate problem.

Table 3: Computational time consumed by the BEM and the LHBIE method for solving the problem of the perforated plate for various types of meshes and for different size of the local domain.

# of Nodes	BEM	LHBIE T-1	LHBIE T-2	LHBIE T-3
364	759s	72s	73s	76s
445	1495s	105s	108s	112s
574	2979s	176s	180s	186s
738	5388s	304s	310s	313s

- The discretization of the analyzed domain is performed by placing boundary and internal nodes. No special discretization rule is required so as to achieve good solution to the problem.
- No MLS approximation or RBF interpolation schemes are utilized (as in most meshless methodologies). The use of the trivial shape functions of one-dimensional elements boosts numerical evaluation of boundary integrals. The stability of the method is not depended by the decision of a weight function, as in meshless interpolation schemes.
- The local domain of integration is constant and defined by the union of "background" triangles. The obtained results of the LHBIE formulation do not depend on any support domain radius decision, as reported in [Atluri, Kim, and Cho (1999); Vavourakis, Sellountos, and Polyzos (2006)] for the MLPG and LBIE methodologies.
- Very fast numerical computation of boundary integrals compared to the corresponding integrals of the BEM (local integration on triangular faces and not on global boundary Γ), and faster to most MLPG formulations proposed so far.
- Displacements and stresses are treated as independent variables by using an isoparametric interpolation, as seen in Eq. (13).
- Direct evaluation of stresses with relative accuracy as with displacements.
- Matrix A_{ij} is $5N \times 5N$ instead of $2N \times 2N$ in conventional BEM. Matrix is banded and not fully-populated or sparse, which leads to significantly faster solutions of the final linear system when comparable degrees-of-freedom with the BEM is the case.

- The proposed method is sensitive to near hypersingularities, met only in the integrals over the local boundary $\partial\Omega_{(\kappa)}$. Special treatment must be taken into account [Bu and Davies (1995); Bu (1997); Yang (2000)].
- The same formulation can be carried out so as to solve time-harmonic problems with the use of volume integrals, as described in paper [Sellountos and Polyzos (2003)].
- The Local Hypersingular Boundary Integral Equation method can be easily expanded for solving three-dimensional problems. It can also be utilized to solve incompressible and nearly incompressible elastic solids, as in paper [Vavourakis and Polyzos (2008)].
- This methodology can be combined with the BEM, in case of multi-region analysis problems with more than one numerical methods being implemented.

5 Conclusions

In the present paper a novel meshless numerical formulation for two-dimensional elastostatics is proposed. The Local Hypersingular Boundary Integral Equation method utilizes a local form of the integral representations of displacements and stresses of the conventional BEM. The analyzed elastic domain is discretized by a distribution of nodes. From this set of nodes it is defined a “background” mesh of triangles. The local domain of each node is considered to be the union of its neighbourhood triangles. In this sub-domain, all local boundary integrals are evaluated, so as to obtain a discrete system of equilibrium equations.

The verification and validity of the proposed methodology is demonstrated by solving three two-dimensional elastostatic examples. The obtained numerical results demonstrate the accuracy and stability of the LHBIE formulation, compared with the BEM.

Acknowledgement: The support of Professors Demosthenes Polyzos and John A. Ekaterinaris during the preparation of this paper is kindly acknowledged.

References

Atluri, S. N.; Han, Z. D.; Rajendran, A. M. (2004): A new implementation of the meshless finite volume method, through the MLPG “Mixed” approach. *CMES: Computer Modeling in Engineering & Sciences*, vol. 6, pp. 491–513.

Atluri, S. N.; Kim, H.-G.; Cho, J. Y. (1999): A critical assessment of the truly Meshless Local Petrov-Galerkin (MLPG), and Local Boundary Integral Equation (LBIE) methods. *Computational Mechanics*, vol. 24, pp. 348–372.

Atluri, S. N.; Shen, S. (2002): The Meshless Local Petrov-Galerkin (MLPG) Method: A Simple & Less-costly Alternative to the Finite Element and Boundary Element Methods. *CMES: Computer Modeling in Engineering & Sciences*, vol. 3, pp. 11–51.

Atluri, S. N.; Sladek, J.; Sladek, V.; Zhu, T. (2000): The local boundary integral equation (LBIE) and it's meshless implementation for linear elasticity. *Computational Mechanics*, vol. 25, pp. 180–198.

Atluri, S. N.; Zhu, T. (1998): A new meshless local Petrov-Galerkin (MLPG) approach in computation mechanics. *Computational Mechanics*, vol. 22, pp. 117–127.

Banerjee, P. K. (1994): *The Boundary Element Methods in Engineering*. McGraw-Hill.

Belytschko, T.; Lu, Y. Y.; Gu, L. (1994): Element-free Galerkin methods. *International Journal for Numerical Methods in Engineering*, vol. 37, pp. 229–256.

Bodin, A.; Ma, J.; Xin, X. J.; Krishnaswami, P. (2006): A meshless integral method based on regularized boundary integral equation. *Computer Methods in Applied Mechanics and Engineering*, vol. 195, pp. 6258–6286.

Brebbia, C. A.; Dominguez, J. (1998): *Boundary Elements: An Introductory Course*. Computational Mechanics Publications, Southampton.

Bu, S. (1997): Infinite boundary elements for the dynamic analysis of machine foundations. *International Journal for Numerical Methods in Engineering*, vol. 40, pp. 3901–3917.

Bu, S.; Davies, T. G. (1995): Effective evaluation of non-singular integrals in 3D BEM. *Advances in Engineering Software*, vol. 23, pp. 121–128.

Chen, J. S.; Pan, C.; Wu, C. T.; Liu, W. K. (1996): Reproducing kernel particle methods for large deformation analysis of nonlinear structures. *Computer Methods in Applied Mechanics and Engineering*, vol. 139, pp. 195–227.

Duarte, C. A.; Oden, J. T. (1996): An h-p adaptive method using clouds. *Computer Methods in Applied Mechanics and Engineering*, vol. 139, pp. 237–262.

Frangi, A.; Guiggiani, M. (2000): A direct approach for boundary integral equations with high-order singularities. *International Journal for Numerical Methods in Engineering*, vol. 49, pp. 871–898.

Gingold, R. A.; Moraghan, J. J. (1977): Smoothed particle hydrodynamics: Theory and applications to non-spherical stars. *Monthly Notice of the Royal Astronomical Society*, vol. 18, pp. 375–389.

Guiggiani, M. (1994): Hypersingular formulation for boundary stress evaluation. *Engineering Analysis with Boundary Elements, Special Issue on Integration Techniques*, vol. 13, pp. 169–179.

Guiggiani, M. (1995): Hypersingular boundary integral equations have an additional free term. *Computational Mechanics*, vol. 16, pp. 245–248.

Guiggiani, M.; Krishnasamy, G.; Rudolphi, T. J.; Rizzo, F. J. (1992): A general algorithm for the numerical solution of hypersingular boundary integral equations. *ASME Journal of Applied Mechanics*, vol. 59, pp. 604–614.

Han, Z. D.; Atluri, S. N. (2003a): On simple formulations of Weakly-Singular Traction & Displacement BIE, and their solutions through Petrov-Galerkin approaches. *CMES: Computer Modeling in Engineering & Sciences*, vol. 4, pp. 5–20.

Han, Z. D.; Atluri, S. N. (2003b): Truly Meshless Local Petrov-Galerkin (MLPG) solutions of traction & displacement BIEs. *CMES: Computer Modeling in Engineering & Sciences*, vol. 4, pp. 665–678.

Han, Z. D.; Atluri, S. N. (2007): A Systematic Approach for the Development of Weakly-Singular BIEs. *CMES: Computer Modeling in Engineering & Sciences*, vol. 21, pp. 41–52.

Lancaster, P.; Salkauskas, K. (1981): Surfaces generated by moving least squares methods. *Mathematics of Computations*, vol. 37, pp. 141–158.

Liu, W. K.; Jun, S.; Zhang, Y. F. (1995): Reproducing kernel particle methods. *International Journal for Numerical Methods in Fluids*, vol. 20, pp. 1081–1106.

Melenk, J. M.; Babuška, I. (1996): The partition of unity finite element method: basic theory and applications. *Computer Methods in Applied Mechanics and Engineering*, vol. 139, pp. 289–314.

Mukherjee, S.; Mukherjee, Y. X. (2005): *Boundary Methods: Elements, Contours, and Nodes*. CRC Press, Boca Raton, FL.

Okada, H.; Rajiyah, H.; Atluri, S. N. (1989): Non-hyper-singular integral-representations for velocity (displacement) gradients in elastic/plastic solids (small or finite deformations). *Computational Mechanics*, vol. 4, pp. 165–175.

Polyzos, D.; Tsinopoulos, S. V.; Beskos, D. E. (1998): Static and dynamic boundary element analysis in incompressible linear elasticity. *European Journal of Mechanics, A/Solids*, vol. 17, pp. 515–536.

Sellountos, E. J.; Polyzos, D. (2003): A MLPG (LBIE) method for solving frequency domain elastic problems. *CMES: Computer Modeling in Engineering & Sciences*, vol. 4, pp. 619–636.

Sellountos, E. J.; Polyzos, D. (2005a): A meshless local boundary integral equation method for solving transient elastodynamic problems. *Computational Mechanics*, vol. 35, pp. 265–276.

Sellountos, E. J.; Polyzos, D. (2005b): A MLPG(LBIE) approach in combination with BEM. *Computer Methods in Applied Mechanics and Engineering*, vol. 194, pp. 859–875.

Shewchuk, J. R. (1996): Triangle: Engineering a 2D Quality Mesh Generator and Delaunay Triangulator. In Lin, M. C.; Manocha, D.(Eds): *Applied Computational Geometry: Towards Geometric Engineering*, pp. 203–222. Springer-Verlag.

Shewchuk, J. R. (2002): Delaunay Refinement Algorithms for Triangular Mesh Generation. *Computational Geometry: Theory and Applications*, vol. 22, pp. 21–74.

Sladek, J.; Sladek, V. (2003): Application of local boundary integral equation method into micropolar elasticity. *Engineering Analysis with Boundary Elements*, vol. 27, pp. 81–90.

Sladek, J.; Sladek, V.; Atluri, S. N. (2001): A Pure Contour Formulation for the Meshless Local Boundary Integral Equation Method in Thermoelasticity. *CMES: Computer Modeling in Engineering & Sciences*, vol. 2, pp. 423–434.

Sladek, J.; Sladek, V.; Keer, R. V. (2000): Numerical integration of singularities of local boundary integral equations. *Computational Mechanics*, vol. 25, pp. 394–403.

Sladek, J.; Sladek, V.; Keer, R. V. (2003): Meshless local boundary integral equation method for 2D elastodynamic problems. *International Journal for Numerical Methods in Engineering*, vol. 57, pp. 235–249.

Sladek, J.; Sladek, V.; Krivacek, J.; Zhang, C. (2003): Local BIEM for transient heat conduction analysis in 3-D axisymmetric functionally graded solids. *Computational Mechanics*, vol. 32, pp. 169–176.

Sladek, J.; Sladek, V.; Mang, H. A. (2003): Meshless LBIE formulations for simply supported and clamped plates under dynamic load. *Computers and Structures*, vol. 81, pp. 1643–1651.

Sukumar, N.; Moran, B.; Belytschko, T. (1998): The natural element method in solid mechanics. *International Journal for Numerical Methods in Engineering*, vol. 43, pp. 839–887.

Timoshenko, S. P.; Goodier, J. N. (1970): *Theory of Elasticity*. McGraw-Hill 3rd Edition, New York.

Vavourakis, V.; Polyzos, D. (2006): A MLPG4 (LBIE) formulation for solving axisymmetric problems. In Sladek, J.; Sladek, V.(Eds): *Advances in Meshless Methods*, pp. 291–316. Tech Science Press.

Vavourakis, V.; Polyzos, D. (2007): A MLPG4 (LBIE) formulation in elastostatics. *CMC: Computers, Materials & Continua*, vol. 5, pp. 185–196.

Vavourakis, V.; Polyzos, D. (2008): A MLPG(LBIE) numerical method for solving 2D incompressible and nearly incompressible elastostatic problems. *Communications in Numerical Methods in Engineering*, vol. 24, pp. 281–296.

Vavourakis, V.; Sellountos, E. J.; Polyzos, D. (2006): A comparison study on different MLPG(LBIE) formulations. *CMES: Computer Modeling in Engineering & Sciences*, vol. 13, pp. 171–184.

Wendland, H. (1999): Meshless Galerkin method using radial basis functions. *Mathematics of Computation*, vol. 68, pp. 1521–1531.

Wu, Z. (1995): Compactly supported positive definite radial functions. *Advances in Computational Mathematics*, vol. 4, pp. 283–292.

Yang, S. A. (2000): An investigation into Integral Equation Methods involving Nearly Singular Kernels for Acoustic Scattering. *Journal of Sound and Vibration*, vol. 234, pp. 225–239.

Zhu, T. (1999): A new Meshless Regular Local Boundary Integral Equation (MRLBIE) approach. *Computational Mechanics*, vol. 46, pp. 1237–1252.

Zhu, T.; Zhang, J. D.; Atluri, S. N. (1998): A local boundary integral equation (LBIE) method in computational mechanics and a meshless discretization approach. *Computational Mechanics*, vol. 21, pp. 223–235.

Appendix A: Fundamental Solutions

In this section the fundamental solution to both the displacements and the stresses boundary integral equations are given, as obtained by literature [Banerjee (1994); Polyzos, Tsinopoulos, and Beskos (1998); Brebbia and Dominguez (1998)]

The fundamental solutions of the boundary integral Eq. (3) are the ones below

$$u_{ij}^* = \frac{1}{2\pi\mu} [\Psi \delta_{ij} - X r_{,i} r_{,j}], \tag{19}$$

$$t_{ij}^* = \frac{1}{2\pi} \left[\left(\frac{d\Psi}{dr} - \frac{X}{r} \right) \left(\frac{\partial r}{\partial \hat{n}} \delta_{ij} + \hat{n}_i r_{,j} \right) + \left(Z - \frac{2X}{r} \right) r_{,i} \hat{n}_j + \left(\frac{4X}{r} - 2 \frac{dX}{dr} \right) \frac{\partial r}{\partial \hat{n}} r_{,i} r_{,j} \right], \tag{20}$$

where μ is the shear modulus $\mu = E/(2(1 + \nu))$. The Euclidean distance vector between source point $\mathbf{x}^{(\kappa)}$ and field point \mathbf{y} is denoted with $\mathbf{r} = \mathbf{y} - \mathbf{x}^{(\kappa)}$, and $r \equiv \|\mathbf{r}\|$, $r_{,i} = r_i/r$, $\partial r/\partial \hat{n} \equiv r_{,i} \hat{n}_i$.

The corresponding hypersingular fundamental solutions of Eq. (5) are

$$u_{ijk}^* = \frac{1}{2\pi} \left[\left(\frac{X}{r} - \frac{d\Psi}{dr} \right) \delta_{ij} r_{,k} + \left(\frac{2X}{r} - Z \right) \delta_{ik} r_{,j} + \left(\frac{X}{r} - \frac{d\Psi}{dr} \right) r_{,i} \delta_{jk} + \left(2 \frac{dX}{dr} - \frac{4X}{r} \right) r_{,i} r_{,j} r_{,k} \right], \tag{21}$$

$$t_{ijk}^* = \frac{\mu}{2\pi} \left[\left(\frac{4X}{r^2} - \frac{4Z}{r} \right) \delta_{ik} \hat{n}_j + \left(4 \frac{d^2X}{dr^2} - \frac{20}{r} \frac{dX}{dr} + \frac{32X}{r^2} \right) \frac{\partial r}{\partial \hat{n}} r_{,i} r_{,j} r_{,k} + \left(\frac{3}{r} \frac{dX}{dr} - \frac{6X}{r^2} - \frac{d^2\Psi}{dr^2} + \frac{1}{r} \frac{d\Psi}{dr} \right) \frac{\partial r}{\partial \hat{n}} (r_{,i} \delta_{jk} + \delta_{ij} r_{,k}) + \right]$$

$$\begin{aligned} & \left(\frac{3}{r} \frac{dX}{dr} - \frac{6X}{r^2} - \frac{d^2\Psi}{dr^2} + \frac{1}{r} \frac{d\Psi}{dr} \right) (\hat{n}_i r_{,j} r_{,k} + r_{,i} r_{,j} \hat{n}_k) + \\ & \left(\frac{4}{r} \frac{dX}{dr} - \frac{8X}{r^2} + Y \right) \left(\frac{\partial r}{\partial \hat{n}} \delta_{ik} r_{,j} + r_{,i} \hat{n}_j r_{,k} \right) + \\ & \left. \left(\frac{2X}{r^2} - \frac{2}{r} \frac{d\Psi}{dr} \right) (\hat{n}_i \delta_{jk} + \delta_{ij} \hat{n}_k) \right]. \end{aligned} \tag{22}$$

The terms in kernels of Eqs. (19), (20) and Eqs. (21), (22) are the following

$$\Psi = \frac{4\bar{\nu} - 3}{4(1 - \bar{\nu})} \ln(r), \quad X = -\frac{1}{4(1 - \bar{\nu})}, \tag{23a}$$

$$\frac{d\Psi}{dr} = \frac{4\bar{\nu} - 3}{4(1 - \bar{\nu})} \frac{1}{r}, \quad \frac{dX}{dr} = 0, \tag{23b}$$

$$\frac{d^2\Psi}{dr^2} = \frac{3 - 4\bar{\nu}}{4(1 - \bar{\nu})} \frac{1}{r^2}, \quad \frac{d^2X}{dr^2} = 0, \tag{23c}$$

$$Z = \frac{\bar{\nu}}{\bar{\nu} - 1} \frac{1}{r}, \tag{23d}$$

$$Y = \frac{4\bar{\nu}}{\bar{\nu} - 1} \frac{1}{r^2}, \tag{23e}$$

where the modified Poisson ratio is

$$\bar{\nu} = \begin{cases} \nu, & \text{for plane-strain} \\ \frac{\nu}{1+\nu}, & \text{for plane-stress} \end{cases}. \tag{24}$$

Appendix B: Free-term coefficient arrays

In this section the analytical expressions of the free-term coefficient arrays of boundary integral equations (3) and (5) are given in detail.

The symmetric matrix of the free-term coefficient of the singular boundary integral Eq. (3) of displacements is [Guiggiani, Krishnasamy, Rudolphi, and Rizzo (1992); Mukherjee and Mukherjee (2005)]

$$\alpha_{ij} = \lim_{V_\varepsilon \rightarrow 0} \left\{ \int_{\Gamma_{(\kappa)s}} u_{ij}^* (\mathbf{x}^{(\kappa)}, \mathbf{y}) dS_{\mathbf{y}} \right\}, \tag{25}$$

where the local boundary $\Gamma_{(\kappa)s}$ is depicted in Fig. 2.

The corresponding free-term coefficient tensors of the hypersingular boundary integral Eq. (5) of stresses are [Guiggiani (1995)]

$$a_{ijkl} = \lim_{V_\varepsilon \rightarrow 0} \left\{ \int_{\Gamma_{(\kappa)s}} \left[t_{ijk}^* (\mathbf{x}^{(\kappa)}, \mathbf{y}) (y_l - x_l^{(\kappa)}) - u_{ijk}^* (\mathbf{x}^{(\kappa)}, \mathbf{y}) \hat{n}_l(\mathbf{y}) \right] dS_{\mathbf{y}} \right\}, \tag{26}$$

and

$$b_{ijk} = \lim_{V_\varepsilon \rightarrow 0} \left\{ \int_{\Gamma_{(\kappa)S}} t_{ijk}^* (\mathbf{x}^{(\kappa)}, \mathbf{y}) dS_{\mathbf{y}} \right\}. \quad (27)$$

where \hat{n}_l is the component of the outward unit normal vector to $\Gamma_{(\kappa)S}$, where field point \mathbf{y} lies.

In the special case when $\mathbf{x}^{(\kappa)}$ lies on a smooth boundary or inside the domain Ω of the analyzed body, then all elements of array b_{ijk} are equal to zero.